Supplemental Document

Phase-cycling and double-quantum two-dimensional electronic spectroscopy using a common-path birefringent interferometer: supplement

Daniel Timmer,[1] Daniel C. Lünemann,[1] Moritz Gittinger,[1] Antonietta De Sio,[1,2] Cristian Manzoni,[3] Giulio Cerullo,[3,4] and Christoph Lienau[1,2,*]

[1] *Institut für Physik, Carl von Ossietzky Universität Oldenburg, 26129 Oldenburg, Germany*
[2] *Center for Nanoscale Dynamics (CENAD), Carl von Ossietzky Universität Oldenburg, 26129 Oldenburg, Germany*
[3] *Istituto di Fotonica e Nanotecnologie-CNR, Piazza L. da Vinci 32, 20133 Milano, Italy*
[4] *Dipartimento di Fisica, Politecnico di Milano, Piazza L. da Vinci 32, 20133 Milano, Italy*
[*] *christoph.lienau@uni-oldenburg.de*

Supplement DOI: https://doi.org/10.6084/m9.figshare.27853911

Parent Article DOI: https://doi.org/10.1364/OPTICA.543007

PHASE-CYCLING AND DOUBLE-QUANTUM TWO-DIMENSIONAL ELECTRONIC SPECTROSCOPY USING A COMMON-PATH BIREFRINGENT INTERFEROMETER: SUPPLEMENTAL DOCUMENT

1. Analytical calculations of Phase-Cycling in TWINS

The Translating Wedge-based Identical pulse eNcoding System (TWINS) [1-3] is a common-path in-line interferometer based on birefringent wedges that allows to produce a highly phase-stable pulse pair with precisely tunable delay τ. It consists of a single block and two pairs of wedges that are cut such that the optical axis is aligned along different orientations [2]. As shown in Fig. 1 of the main manuscript, the first block has its optical axis aligned in Y-direction (see Fig. 1 for coordinate system). For the two wedge pairs, the optical axis is aligned in X direction and Z direction, respectively. Behind the TWINS, a polarizer oriented at 45° with respect to the Y-axis is used to project the two pulses that are polarized at 0° and 90° onto the same polarization direction (Fig. 1). The working principle of the TWINS is described in Refs. [2] and [3] and in the main manuscript. To tune the delay τ, two wedges, one of each pair (one X-cut and one Z-cut wedge), are synchronously moved in or out by a translation x, such that the total material thickness through which the laser beam passes remains constant. The movement is almost perpendicular to the laser propagation direction, tilted by the apex angle. This way the optical phase acquired by the vertically polarized contribution (pulse 2) remains unchanged. In contrast, for the horizontally polarized contribution (pulse 1) the relative thickness of the material with ordinary and extraordinary refractive index is altered, introducing a group delay. In our case, α-BBO is used as the birefringent material. We assume that initially the input pulse is linearly polarized at 0°. Then, either a polarizer or a half-wave plate can be used to create the input pulse linearly polarized at 45°, which is assumed as input state in Ref. [2]. For this, we use a polarizer both in experiment and in the following calculations. An increased total interferometer throughput can, in principle, be achieved by using a half-wave plate instead. In the following, we simulate the effects of the TWINS interferometer on the polarization properties of the input pulse while also considering phase effects. For simplicity, we neglect any phase changes introduced by the optical components that affect both polarization components identically. Such phase effects include a group delay and dispersion effects of the polarizers, quarter-wave plate and TWINS. Since these phases affect both pulse 1 and 2 (Fig. 1), their effect will not be considered. Also, effects of spatial beam propagation, reflection losses, manufacturing tolerances and alignment are not considered.

1.1 Conventional TWINS

We calculate the effects of the individual optical components of the TWINS interferometer on the input electric field using Jones Calculus [4, 5]. Here, the polarization state of light is described by its horizontal and vertical components. We assume the incident light to be vertically polarized:

$$\vec{E}_{in} = E_{in}\begin{bmatrix}0\\1\end{bmatrix} \tag{S1}$$

The effect of optical components on this polarization state is modeled by a multiplication with a suitable Jones matrix. For a linear polarizer with its axis of transmission aligned vertically, this matrix reads

$$P = \begin{bmatrix}0 & 0\\0 & 1\end{bmatrix}. \tag{S2}$$

A quarter-wave plate (QWP) with its fast axis aligned vertically can be described by [5]

$$Q = \begin{bmatrix} i & 0 \\ 0 & 1 \end{bmatrix}. \tag{S3}$$

If these optics are rotated by an angle φ from the vertical, a rotation matrix

$$R(\varphi) = \begin{bmatrix} \cos(\varphi) & -\sin(\varphi) \\ \sin(\varphi) & \cos(\varphi) \end{bmatrix}. \tag{S4}$$

needs to be multiplied to both, from each side, resulting in the following generalized expressions for a polarizer and a quarter-wave plate, rotated from the vertical [5]:

$$P(\varphi) = R^T(\varphi) P R(\varphi) = \begin{bmatrix} \sin^2(\varphi) & \sin(\varphi)\cos(\varphi) \\ \sin(\varphi)\cos(\varphi) & \cos^2(\varphi) \end{bmatrix}, \tag{S5}$$

$$Q(\vartheta) = R^T(\vartheta) Q R(\vartheta) = \begin{bmatrix} \sin^2(\vartheta) + i\cos^2(\vartheta) & (1-i)\sin(\vartheta)\cos(\vartheta) \\ (1-i)\sin(\vartheta)\cos(\vartheta) & \cos^2(\vartheta) + i\sin^2(\vartheta) \end{bmatrix}. \tag{S6}$$

The five α-BBO crystals of the TWINS introduce, in total, a relative phase difference $\phi_{TWINS}(x,\omega) = -\omega c_0^{-1} \Delta n(\omega) \sin(\alpha) x$ between the two polarization components in the interferometer. This phase difference depends on the position x of the TWINS wedges (Fig. 1), their opening angle ($\alpha = 7°$), the speed of light in vacuum c_0 and the color-dependent difference between the ordinary (n_o) and extraordinary (n_e) refractive indices of α-BBO, $\Delta n(\omega) = n_e(\omega) - n_o(\omega) < 0$ [2, 6]. Here, $x = 0$ is defined such that the combined traversed thickness of the X-cut wedges equals the thickness of the Y-cut block. Hence, an effective Jones matrix for the TWINS reads

$$T(x,\omega) = \begin{bmatrix} e^{-i\phi_{TWINS}(x,\omega)} & 0 \\ 0 & 1 \end{bmatrix}. \tag{S7}$$

The electric field $\vec{E}_{out}$ behind the complete TWINS system, consisting of a first polarizer (45°), the TWINS crystals and a second polarizer (45°) is described by

$$\begin{aligned} \vec{E}_{out}(x,\omega) &= P(+45°) T(x,\omega) P(+45°) \vec{E}_{in} = \frac{E_{in}}{4}\left(e^{-i\phi_{TWINS}(x,\omega)} + 1\right)\begin{bmatrix} 1 \\ 1 \end{bmatrix} \\ &=: \vec{E}_1(x,\omega) + \vec{E}_2. \end{aligned} \tag{S8}$$

This creates two output pulses with individual field components $\vec{E}_1(x,\omega) = \frac{1}{4} E e^{i\phi_{TWINS}(x,\omega)} \begin{bmatrix} 1 \\ 1 \end{bmatrix}$ and $\vec{E}_2 = \frac{1}{4} E \begin{bmatrix} 1 \\ 1 \end{bmatrix}$. The subscripts 1 and 2 indicate whether the respective pulse arrives first or second for $\tau > 0$, respectively. With this we determine the phase difference $\Delta\phi(\omega) = \phi_2(\omega) - \phi_1(\omega)$ between pulse 1 and pulse 2, the average intensity I_{avg} and the fringe contrast C behind the TWINS:

$$\Delta\phi(x,\omega) = \arg\left(\vec{E}_1^*(x,\omega) \cdot \vec{E}_2\right) = \phi_{TWINS}(x,\omega) \tag{S9}$$

$$I_{avg} = \left|\vec{E}_1(x,\omega)\right|^2 + \left|\vec{E}_2\right|^2 = \frac{1}{4}E^2 \tag{S10}$$

$$C = \frac{I_{max} - I_{avg}}{I_{avg}} = \frac{2\left|\vec{E}_1^*(x,\omega) \cdot \vec{E}_2\right|}{\left|\vec{E}_1(x,\omega)\right|^2 + \left|\vec{E}_2\right|^2} = 1 \tag{S11}$$

Thus, the conventional TWINS operates at a fixed average throughput efficiency of 25% and with full contrast. For linearly polarized input pulses, the throughput can be increased to 50% by exchanging the first polarizer by a half-wave plate (HWP).

1.2 Phase-cycling TWINS

In order to adapt the TWINS for phase cycling, a QWP is added either in front of or behind the TWINS crystals but, importantly, in-between the two polarizers. For full phase control, the second polarizer is now allowed to be either tuned to +45° or -45°. A third polarizer, added behind the second polarizer and set to transmit vertically polarized light, ensures that this does not affect the output polarization. The new output field of the phase-cycling (PC) TWINS therefore reads

$$\vec{E}_{out}^{PC}(x,\omega,\vartheta) = P(0°)P(\pm 45°)Q(\vartheta)T(x,\omega)P(+45°)\vec{E}_{in} = \vec{E}_1^{PC}(x,\omega,\vartheta) + \vec{E}_2^{PC}(\quad \text{(S12)}$$

with

$$\vec{E}_1^{PC}(x,\omega,\vartheta) = \pm\frac{1-\cos(2\vartheta)\pm\sin(2\vartheta)+i\big(1+\cos(2\vartheta)\mp\sin(2\vartheta)\big)}{8}e^{-i\phi_{TWINS}(x, \quad \text{(S13)}$$

$$\vec{E}_2^{PC}(\vartheta) = \frac{1+\cos(2\vartheta)\pm\sin(2\vartheta)+i\big(1-\cos(2\vartheta)\mp\sin(2\vartheta)\big)}{8}\vec{E}_{in}. \quad \text{(S14)}$$

Equations (S13) and (S14) are the central result of this work. They show that, after introducing the QWP, the time delay between pulses 1 and 2 is still defined by the spectral phase $\phi_{TWINS}(x,\omega)$ introduced by the wedge pairs and, thus can be controlled by translating the wedge pairs. In addition, the frequency-independent absolute phase of the two pulses can now be controlled by varying the rotation angle ϑ of the QWP.

These output field components now allow us to calculate the phase difference $\Delta\phi^{PC}(x,\omega)$, average intensity $I_{avg}^{PC}(\vartheta)$ and fringe contrast $C^{PC}(\vartheta)$ for the PC-TWINS. Firstly, the phase introduced by the second polarizer is introduced explicitly by replacing the prefix " $\pm$ " in the expression for $\vec{E}_1^{PC}(x,\omega,\vartheta)$ by $e^{i\phi_{pol}}$ with

$$\phi_{pol} = \begin{cases} 0, & \text{second polarizer at } +45° \\ \pi, & \text{second polarizer at } -45°. \end{cases} \quad \text{(S15)}$$

This simplifies the field contributions to

$$\vec{E}_1^{PC}(x,\omega,\vartheta) = \frac{1}{8}\mathcal{E}_1(\vartheta)e^{i\phi_{pol}-i\phi_{TWINS}(x,\omega)}\vec{E}_{in}, \vec{E}_2^{PC}(\vartheta) = \frac{1}{8}\mathcal{E}_2(\vartheta)\vec{E}_{in} \quad \text{(S16)}$$

with

$$\mathcal{E}_1(\vartheta) = 1-\cos(2\vartheta)\pm\sin(2\vartheta)+i\big(1+\cos(2\vartheta)\mp\sin(2\vartheta)\big), \quad \text{(S17)}$$

$$\mathcal{E}_2(\vartheta) = 1+\cos(2\vartheta)\pm\sin(2\vartheta)+i\big(1-\cos(2\vartheta)\mp\sin(2\vartheta)\big). \quad \text{(S18)}$$

These expressions isolate the phase and amplitude changes introduced by the QWP onto each pulse replica. These expressions are still depending on the second polarizer orientation, as seen in the " $\pm$ ". From these, the relative phase $\phi_{QWP}(\vartheta)$ introduced by the QWP can be deduced,

$$\phi_{QWP}(\vartheta) = \arg(\mathcal{E}_2(\vartheta)) - \arg(\mathcal{E}_1(\vartheta)) = \arg(\mathcal{E}_1^*(\vartheta)\mathcal{E}_2(\vartheta)) = -\arctan\left(\frac{\cos}{\sin} \quad \text{(S19)}$$

which is independent from the second polarizer's orientation. With this, we finally obtain the full relative phase $\Delta\phi^{PC}(x,\omega,\vartheta)$ induced by the Phase-cycling TWINS:

$$\begin{aligned}\Delta\phi^{PC}(x,\omega,\vartheta) &= \arg\left(\vec{E}_1^{PC*}(x,\omega,\vartheta)\cdot\vec{E}_2^{PC}(\vartheta)\right) = \phi_{TWINS}(x,\omega)+\phi_{QWP}(\vartheta)+\phi_{} \\ &= \phi_{TWINS}(x,\omega)+\Delta\phi_0\end{aligned} \tag{S20}$$

The PC-TWINS therefore introduces a time delay $\tau(x)=\left.\frac{\partial\phi_{TWINS}(x,\omega)}{\partial\omega}\right|_{\omega_L}$ between the two pulses in the interferometer (ω_L: center frequency of the laser pulses) but, importantly, also allows to imprint a controllable difference in absolute phase $\Delta\phi_0$ onto this pulse pair. Eq. (S20) shows that this phase difference is given as $\Delta\phi_0=\phi_{QWP}(\vartheta)+\phi_{pol}$.

Ultimately, also the amplitude changes in $\mathcal{E}_1$ and $\mathcal{E}_2$ can be used to determine the average intensity I_{avg}^{PC} and contrast $C^{PC}(\vartheta)$ of the Phase-cycling TWINS as a function of the QWP orientation:

$$I_{avg}^{PC}=\left|\vec{E}_1^{PC}(x,\omega,\vartheta)\right|^2+\left|\vec{E}_2^{PC}(\vartheta)\right|^2=\frac{|\mathcal{E}_1(\vartheta)|^2+|\mathcal{E}_2(\vartheta)|^2}{64}E_{in}^2=\frac{1}{8}E_{in}^2 \tag{S21}$$

$$C^{PC}(\vartheta)=\frac{2\left|\vec{E}_1^{PC*}(x,\omega,\vartheta)\cdot\vec{E}_2^{PC}(\vartheta)\right|}{\left|\vec{E}_1^{PC}(x,\omega,\vartheta)\right|^2+\left|\vec{E}_2^{PC}(\vartheta)\right|^2}=\frac{2|\mathcal{E}_1(\vartheta)\mathcal{E}_2(\vartheta)|}{|\mathcal{E}_1(\vartheta)|^2+|\mathcal{E}_2(\vartheta)|^2}=\sqrt{1-\frac{1}{4}\sin^2(4} \tag{S22}$$

Most importantly, the PC-TWINS can introduce all possible relative phases $\Delta\phi_0$ between the two pulses. The QWP alone only covers phases between $-\pi/2$ and $\pi/2$. The second polarizer, which introduces the "$\pm$" in Eq. (S13), causes a relative sign flip between the two pulses which is unaffected by the QWP angle. This corresponds to a relative phase of π. In combination, all phase values are covered.

The throughput of the PC-TWINS is independent of the induced phase. In comparison to the conventional TWINS it is reduced by a factor of 2 to 12.5% due to the additional polarizer. The use of a HWP instead of the first polarizer could increase the throughput to 25%. When also using a HWP instead of the third polarizer, the throughput could be further increased to 50%. In this case, however, the orientation of the HWP instead of the third polarizer would have to be adapted to the second polarizer's orientation to ensure a constant polarization in the experiment.

The interference contrast of the PC-TWINS is modulated between 1 and 0.866 as a function of the QWP orientation. Importantly, a contrast of 1 is achieved for phases that are integer multiples of $\pi/4$. In order to achieve maximum contrast of 1 for all QWP orientations and thus for all applied phases the first polarizer's transmission axis (φ) can be utilized, yielding

$$\vec{E}_{out}^{PC}(x,\omega,\vartheta,\varphi)=\cos^2(\varphi)\left(\tan(\varphi)\,\vec{E}_1^{PC}(x,\omega,\vartheta)+\vec{E}_2^{PC}(\vartheta)\right). \tag{S23}$$

When setting

$$\varphi(\vartheta)=\arctan\left(\sqrt{\frac{1\pm\frac{1}{2}\sin(4\vartheta)}{1\mp\frac{1}{2}\sin(4\vartheta)}}\right), \tag{S24}$$

$C^{PC}\equiv 1$ is achieved. This, however, comes at the cost of a ϑ-dependent average intensity,

$$I_{avg}^{PC}(\vartheta)=\cos^4(\varphi(\vartheta))\left[\tan^2(\varphi(\vartheta))\left|\vec{E}_1^{PC}(x,\omega,\vartheta)\right|^2+\left|\vec{E}_2^{PC}(\vartheta)\right|^2\right] \tag{S25}$$

2. Response function based 2DES simulations

To simulate rephasing and non-rephasing single-quantum (1Q) as well as double-quantum (2Q) and zero-quantum (0Q) 2DES spectra we employ a response function approach [7-9]. This perturbative approach allows us to compare the experimental data to a minimal set of quantum pathways via their respective third-order nonlinear response function. The double-sided Feynman diagrams that are the basis for these response functions are depicted in Fig. 3 for the 1Q pathways and in Fig. 4 for the 2Q and 0Q spectra.

We assume a three-level system (3LS) with a ground state $|0\rangle$, first excited state $|1\rangle$ and doubly excited state $|2\rangle$. We denote the energy difference between ground and first excited state as $E_{01} = \hbar\omega_{01}$ and between the first and doubly excited state as $E_{12} = \hbar\omega_{12}$. We assign a transition dipole moment of μ_{01} to the transition between $|0\rangle$ and $|1\rangle$ and μ_{12} between $|1\rangle$ and $|2\rangle$.

For the 1Q spectra, we get a total of six third-order response functions. These contain three non-rephasing and three rephasing contributions reflecting stimulated emission (SE), ground state bleaching (GSB) and excited state absorption (ESA) The corresponding Feynman diagrams are depicted in Fig. 3c in the main manuscript.

$$
\begin{aligned}
R_{SE}^{NR}(t,\tau,T) &= (-1)^2\left(\frac{i}{\hbar}\right)^3 \mu_{01}^4 e^{-i\omega_{01}\tau} e^{-\tau/T_2^{01}} e^{-T/T_1} e^{-i\omega_{01}t} e^{-t/T_2^{01}} \\
R_{GSB}^{NR}(t,\tau,T) &= (-1)^0\left(\frac{i}{\hbar}\right)^3 \mu_{01}^4 e^{-i\omega_{01}\tau} e^{-\tau/T_2^{01}} e^{-T/T_1} e^{-i\omega_{01}t} e^{-t/T_2^{01}} \\
R_{ESA}^{NR}(t,\tau,T) &= (-1)^1\left(\frac{i}{\hbar}\right)^3 \mu_{01}^2\mu_{12}^2 e^{-i\omega_{01}\tau} e^{-\tau/T_2^{01}} e^{-T/T_1} e^{-i\omega_{12}t} e^{-t/T_2^{12}} \\
R_{SE}^{R}(t,\tau,T) &= (-1)^2\left(\frac{i}{\hbar}\right)^3 \mu_{01}^4 e^{+i\omega_{01}\tau} e^{-\tau/T_2^{01}} e^{-T/T_1} e^{-i\omega_{01}t} e^{-t/T_2^{01}} \\
R_{GSB}^{R}(t,\tau,T) &= (-1)^2\left(\frac{i}{\hbar}\right)^3 \mu_{01}^4 e^{+i\omega_{01}\tau} e^{-\tau/T_2^{01}} e^{-T/T_1} e^{-i\omega_{01}t} e^{-t/T_2^{01}} \\
R_{ESA}^{R}(t,\tau,T) &= (-1)^1\left(\frac{i}{\hbar}\right)^3 \mu_{01}^2\mu_{12}^2 e^{+i\omega_{01}\tau} e^{-\tau/T_2^{01}} e^{-T/T_1} e^{-i\omega_{12}t} e^{-t/T_2^{12}}
\end{aligned}
\tag{S26}
$$

These response functions depend on the three delays t,τ and T which are the detection time, coherence time and waiting time, respectively. We use 1Q electronic dephasing times T_2^{01} and T_2^{12} to account for the linewidth of the $|0\rangle\leftrightarrow|1\rangle$ and $|1\rangle\leftrightarrow|2\rangle$ coherences, respectively, while T_1 describes population relaxation dynamics.

For the 2Q spectra, we use the following response functions:

$$
\begin{aligned}
R_1^{2Q}(t,\tau,T) &= (-1)^0\left(\frac{i}{\hbar}\right)^3 \mu_{01}^2\mu_{12}^2 e^{-i(\omega_{01}+\omega_{12})\tau} e^{-\tau/T_2^{02}} e^{-i\omega_{01}T} e^{-T/T_2^{01}} e^{-i\omega_{01}t} e^{-} \\
R_2^{2Q}(t,\tau,T) &= (-1)^1\left(\frac{i}{\hbar}\right)^3 \mu_{01}^2\mu_{12}^2 e^{-i(\omega_{01}+\omega_{12})\tau} e^{-\tau/T_2^{02}} e^{-i\omega_{01}T} e^{-T/T_2^{01}} e^{-i\omega_{12}t} e^{-}
\end{aligned}
\tag{S27}
$$

These response functions account for the new time ordering that corresponds to the experimental conditions as illustrated in Fig. 4. The 2Q coherence between $|0\rangle$ and $|2\rangle$ decays exponentially with T_2^{02}.

Lastly, the 0Q spectra are calculated using

$$R_{SE}^{0Q}(t,\tau,T) = (-1)^2\left(\frac{i}{\hbar}\right)^3 \mu_{01}^4 e^{-\tau/T_1} e^{-i\omega_{01}T} e^{-T/T_2^{01}} e^{-i\omega_{01}t} e^{-t/T_2^{01}}$$

$$R_{GSB}^{0Q}(t,\tau,T) = (-1)^0\left(\frac{i}{\hbar}\right)^3 \mu_{01}^4 e^{-\tau/T_1} e^{-i\omega_{01}T} e^{-T/T_2^{01}} e^{-i\omega_{01}t} e^{-t/T_2^{01}} \tag{S28}$$

$$R_{ESA}^{0Q}(t,\tau,T) = (-1)^1\left(\frac{i}{\hbar}\right)^3 \mu_{01}^2\mu_{12}^2 e^{-\tau/T_1} e^{-i\omega_{01}T} e^{-T/T_2^{01}} e^{-i\omega_{12}t} e^{-t/T_2^{12}}$$

These response functions are only half of those contributing to the total response [7]. The signal that arises from these response functions has to be real-valued. Therefore, the complex conjugate of each response function is added to calculate the full signal [7, 10]

$$S_{2D}(t,\tau,T) = -2\Re\{iR(t,\tau,T)\} = -i(R(t,\tau,T) - R^*(t,\tau,T)) \tag{S29}$$

Here, $R(t,\tau,T)$ denotes the sum over all contributing response functions. The minus sign reflects the experimental data acquisition scheme of the differential spectra, measuring changes in transmission rather than absorption, while the i describes the phase lag between the sample polarization, described by the response function, and the emitted signal field [7, 10]. Fourier transform along t and τ then yields the 2DES signal

$$\begin{aligned} S_{2D}(\omega_{det},\tau,T) &= \Re\left\{\int_{-\infty}^{\infty} \Theta(t)\, S_{2D}(t,\tau,T) e^{+i\omega_{det}t}\, \mathrm{d}t\right\} \\ S_{2D}(\omega_{det},\omega_{ex},T) &= \int_{-\infty}^{\infty} \Theta(\tau) S_{2D}(\omega_{det},\tau,T) e^{+i\omega_{ex}\tau} \mathrm{d}\tau. \end{aligned} \tag{S30}$$

Here, the Heaviside step function Θ enforces proper pulse ordering and causality along the t and τ axes. Since our measurements are performed in a pump probe geometry, the probe pulse serves as a local oscillator. The restriction to the real part $\Re$ is therefore a consequence of the self-heterodyned detection in a spectrometer using the probe pulse. To separately obtain rephasing and non-rephasing spectra in the simulations, only the respective subset of responses is used to calculate the 2DES signal. While the final signal $S_{2D}(\omega_{det},\omega_{ex},T)$ is complex-valued, usually only the real part is considered since it represents the absorptive lineshape that can be analyzed analogously to a pump-probe nonlinearity [7].

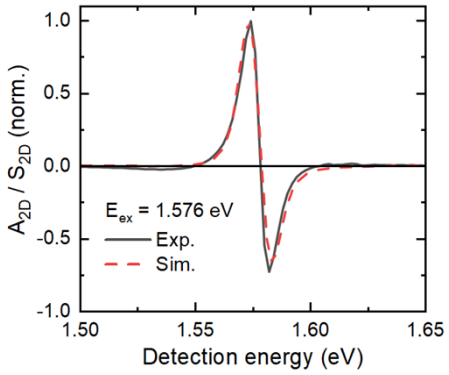

Fig. S1: Comparison between the experimental (black line) and simulated (red dashed line) real-valued absorptive 2DES peak shape at $E_{ex} = 1.576$ eV. Using a dephasing time of $T_2 = 160$ fs for both the 1Q and 2Q transition, a Gaussian inhomogeneous broadening of $\sigma = 2$ meV and a ratio between the 1Q and 2Q transition dipole moments of $\mu_{2Q}/\mu_{1Q} = 0.97\sqrt{2}$ yields good agreement with the experimental data.

Table S1: Simulation parameters

Parameter	Value
E_X	1.576 eV
ΔE	3 meV
T_2^{01}	160 fs
T_2^{12}	160 fs
T_2^{02}	30 fs
T_1	140 fs
σ_{inh}	2 meV
μ_{12}	$0.97\sqrt{2}\mu_{01}$

As in experiment, we only consider $T = 0$ fs for all simulated spectra. When mapping this 3LS onto the J-aggregate sample, we assign $|X\rangle \equiv |1\rangle$ and $|XX\rangle \equiv |2\rangle$ and therefore $\hbar\omega_{01} = E_X$ and $\hbar\omega_{12} = E_X + \Delta E$. To account for the inhomogeneous broadening seen in the experiment, the simulations are repeated while varying E_X by a finite amount δ in steps of 1 meV. All other parameters are kept fixed, including the two-exciton shift ΔE. The results are averaged using a Gaussian distribution with standard deviation σ_{inh}. The value for σ_{inh} was tuned until a good agreement between the signal strength of the rephasing and non-rephasing contributions to the 1Q spectra was achieved (see Fig. 3). The values used in the simulations presented in this work are listed in Table S1. We assume the same electronic dephasing time for the $|0\rangle\leftrightarrow|X\rangle$ and the $|X\rangle\leftrightarrow|XX\rangle$ transitions. All parameters have been tuned to achieve convincing agreement between all simulated and measured 2DES spectra (see Fig. 3 and 4). Fig. S1 demonstrates that the chosen values for E_X, ΔE, μ_{01}, μ_{12}, T_2^{01} and T_2^{12} can accurately reproduce the experimental line shape of the real part of the absorptive 2DES map.

3. Experimental Setup

The experimental setup used for 2DES was previously described by Quenzel et al. [11]. It utilizes a home-built noncollinear optical parametric amplifier [11, 12] (NOPA) that is pumped by a Carbide (Light Conversion) high-repetition rate laser system operating at 200 kHz. It delivers 190-fs pulses (FWHM) centered at 1030 nm. A quarter of the 80 W output is sent to the NOPA. The output spectrum of the NOPA and a measurement of the root-mean square fluctuations (10000 spectra, recorded at a readout rate of 100 kHz) is depicted in Fig. S2.

The NOPA pulses are used in a home-built 2DES setup [11, 13] that operates at 100 kHz repetition rate, i.e. half of the laser repetition rate. This limitation is due to the maximum acquisition rate of the camera used to record the differential spectra of 126 kHz. The NOPA input is split into a pump and probe arm using a beam splitter. An inline interferometer based on birefringent wedges [2] (TWINS) is used to create the phase-stable pump pulse pair. The TWINS can be used to scan the coherence time τ using a motorized translation stage (M112.1DG1, Physik Instrumente). A QWP mounted in a motorized rotation mount and a third polarizer, set to vertical polarization, have been added to control the relative phase $\Delta\varphi$ between the pump pulse replicas, as shown in Fig. 1 of the main manuscript. A fraction of the light behind the TWINS is sent to a photo diode (PD) that can measure a field autocorrelation when a coherence time scan is performed. Chirped mirrors (DCM9, Laser Quantum) are used to compensate additional dispersion introduced by the TWINS. A mechanical chopper system (MC2000B, Thorlabs) that uses a custom-made slotted wheel is used to periodically chop the pump at 50 kHz. The waiting time T between pump and probe is controlled with a retroreflector mounted to a motorized translation stage (M126.DG, Physik Instrumente). Pump and probe are focused onto the sample, located in a vacuum chamber, using an off-axis parabolic mirror (reflected focal length of 150 mm) with a spot size of ~45 x 45 µm². The reflected probe beam

is dispersed using a grating monochromator (Acton SP2150i, Princeton Instruments) and measured with a mounted high-speed line camera (Aviiva EM4, e2v) that records spectra $I(E_{det})$ at a readout rate of 100 kHz. Chopping of the pump (on/off) then results in experimental differential reflectivity spectra

$$A_{2D}(E_{det},\tau,T;\Delta\phi_0) = \frac{\Delta R}{R}(E_{det},\tau,T;\Delta\phi_0) = \frac{I_{on}(E_{det},\tau,T;\Delta\phi_0) - I_{off}(E_{det})}{I_{off}(E_{det})} \quad \text{(S31)}$$

calculated from the probe spectra I_{on} and I_{off} as a function of the detection energy E_{det}, coherence time τ and waiting time T. The spectrally approximately constant relative phase $\Delta\phi_0$ between pump and probe is tuned using the QWP.

All experiments are performed at room temperature with the sample placed under vacuum to avoid possible light-induced degradation effects.

To accurately characterize and optimize the pulse duration used in experiment we use second harmonic frequency-resolved optical gating (SHG-FROG) with a 10-µm β-barium borate (BBO) crystal placed at the intersection between the pump and probe beams in the 2DES setup. First, the pump pulses are characterized utilizing the TWINS interferometer (set to $\Delta\phi_0 = 0$) to collinearly measure an interferometric FROG [14, 15] trace which allows us to extract a SHG-FROG via Fourier filtering. Fig. S2a depicts this Fourier filtered trace as the TWINS-FROG. The stage position axis is converted to group delay using the known frequency-dependent birefringence $\Delta n(\omega)$ of the α-BBO crystals. At 800 nm the TWINS introduces a group delay of $\tau_g \approx 53$ fs per mm stage translation. A retrieved pulse duration of ~10 fs is obtained using a FROG retrieval algorithm (FROG 3.2.2, Femtosoft Technologies).

After pump pulse optimization, a noncollinear cross-correlation SHG-FROG between the pump and probe is measured and the probe dispersion is tuned to achieve a vertical, symmetric FROG trace with minimal temporal width. Fig. S2b depicts this cross-correlation SHG-FROG. It closely resembles the pump FROG obtained from the collinear interferometric measurement. The retrieved pulse duration of ~10.5 fs is close to that obtained for the pump pulse. This demonstrates that optimal pump and probe pulses are both available in the 2DES experiment.

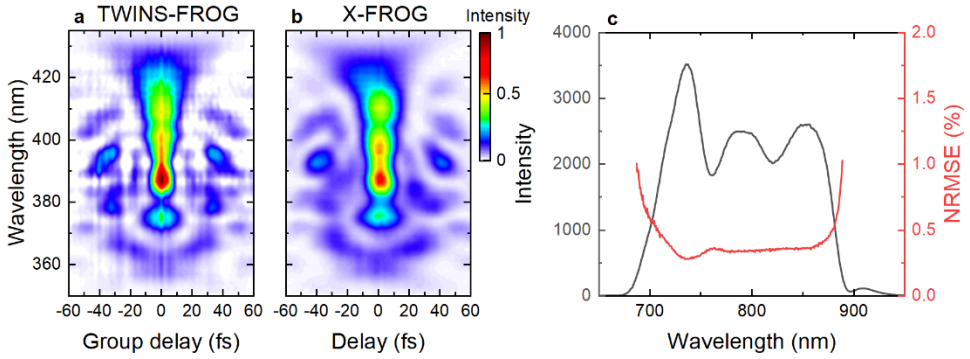

Fig. S2: Laser pulse characterization. (a) TWINS-based SHG-FROG measurement of the pump pulse. (b) Cross-correlation SHG-FROG between pump and probe at the sample position. Both traces yield a retrieved pulse duration of 10 fs. (c) Laser spectrum and single-shot RMS fluctuations.

4. Phase-cycling data evaluation to obtain rephasing, non-rephasing, 0Q and 2Q spectra

4.1 TWINS calibration

In contrast to, e.g., a Michelson or Mach-Zehnder interferometer, the TWINS does not create a phase that is linear in frequency, i.e. a wavelength-independent phase velocity, when moving the interferometer stage. Instead, translation of the wedges for a τ-scan creates a phase term $\phi_{TWINS}(\omega) = -\omega c_0^{-1}\Delta n(\omega)\sin(\alpha)x$ with a more complex spectral dependence that is defined by the birefringence $\Delta n(\omega)$. This frequency-dependence of the delay axis needs to be taken into account in order to obtain the excitation energy axis for a 2DES map [2, 3]. For this, we record a calibration scan. In this scan, the interference spectrum of the excitation pulse pair is measured using a calibrated spectrometer as a function of stage position x for identical settings as in a 2DES coherence time scan. The resulting interferogram is then Fourier transformed along the delay spatial axis x. For each wavelength, the peak position is obtained along the spatial frequency axis of the Fourier transform. This gives the spatial fringe frequency $\Delta k(\omega) = \omega c_0^{-1}\Delta n(\omega)\sin(\alpha)$ [2]. The resulting function relates this spatial modulation frequency to the optical frequency and can therefore be used to convert the Fourier transform axis in a 2DES scan into the excitation energy axis by fitting a low-order polynomial to $\Delta k(\omega)$.

4.2 Measured datasets

For the data presented in the manuscript, we measure $A_{2D}(E_{det},\tau,T;\Delta\phi_0)$ at $T = 0$. The coherence time τ is scanned for relative phase differences of $\Delta\phi_0 = [0,\pi/2]$, realizing a two-step phase-cycling scheme. Alternatively, phase differences of $\Delta\phi_0 = [0,-\pi/2]$ could also be used but would require corresponding adjustments in the following data evaluation, as indicated where necessary.

4.3 Rephasing and non-rephasing spectra

To disentangle the rephasing (R) and non-rephasing (NR) contributions to the 2DES spectra, we follow the procedure described by J. Ogilvie and coworkers [16]. First, we enforce causality along the detection time t in both datasets by inversely Fourier-transforming the raw data along E_{det}, setting all data at negative times equal to zero and Fourier-transforming back to the energy domain,

$$\begin{aligned} A_{2D}(t,\tau,T;\Delta\phi_0) &= \frac{1}{2\pi\hbar}\int_{-\infty}^{\infty} A_{2D}(E_{det},\tau,T;\Delta\phi_0)e^{-i\frac{t}{\hbar}E_{det}}\mathrm{d}E_{det} \\ A'_{2D}(E_{det},\tau,T;\Delta\phi_0) &= \int_{-\infty}^{\infty} \Theta(t)A_{2D}(t,\tau,T;\Delta\phi_0)e^{+i\frac{E_{det}}{\hbar}t}\mathrm{d}t\,, \end{aligned} \tag{S32}$$

with Θ being the Heaviside step function. In Eq. (S30), the complex conjugate of the rephasing and non-rephasing responses have effectively been added by measuring only the real part of the signal A_{2D}. These signals are now removed by imposing causality and we obtain the complex-valued causality-enforced 2DES signal A'_{2D}.

When calculating A'_{2D}, the excitation energy axis is obtained by performing a Fourier-transform along the coherence time. In practice, the Fourier transform is performed along the spatial delay axis x and the calibration curve $\Delta k(\omega)$ measured in the calibration scan of the TWINS is used to deduce the excitation energy axis. For further data processing only data A'_{2D} for $\tau > 0$ are considered, giving the complex-valued and causality-enforced 2DES signal

$$A^{+}_{2D}(E_{det},E_{ex},T;\Delta\phi_0) = \int_{-\infty}^{\infty} \Theta(\tau)A'_{2D}(E_{det},\tau,T;\Delta\phi_0)e^{+i\frac{E_{ex}}{\hbar}\tau}\mathrm{d}\tau\,. \tag{S33}$$

This signal is comprised of rephasing and non-rephasing contributions. The interactions with the two pump pulses, once with the field directly and once with the conjugate field, imprint potential phase differences $\Delta\phi(E_{ex})$ between the two pump pulses onto these measured signals, but with opposing sign due to the different ordering of these interactions,

$$A_{2D}^{+}(E_{det},E_{ex},T;\Delta\phi_0) = A_{2D}^{R}(E_{det},E_{ex},T)e^{-i\Delta\phi(E_{ex})} + A_{2D}^{NR}(E_{det},E_{ex},T)e^{+i\Delta\phi(E_{ex})}. \quad \text{(S34)}$$

This phase difference $\Delta\phi(E_{ex}) = \Delta\phi_0 + \delta\phi(E_{ex})$ can result from the difference in absolute phase $\Delta\phi_0$ that is introduced in the PC-TWINS. Additionally, residual phase differences $\delta\phi(E_{ex})$ may result from non-ideal TWINS alignment and/or components. If needed, the latter can be corrected for by using a field autocorrelation measurement that is recorded simultaneously to the 2DES coherence time scans at $\Delta\phi_0 = 0$. Such a measurement retrieves $\delta\phi(E_{ex})$ from its Fourier transform and allows to correct for them by multiplying the data by $e^{-i\delta\phi(E_{ex})}$. As the autocorrelation is real-valued, this correction term already takes into account the different signs for the rephasing signals (at $E_{ex} < 0$) and non-rephasing signals (at $E_{ex} > 0$). Since the residual phase fluctuations are small (Fig. 2), no such additional phase correction was applied to the experimental data presented in the manuscript. This leaves only the constant phase terms:

$$A_{2D}^{+}(E_{det},E_{ex},T;\Delta\phi_0) = A_{2D}^{R}(E_{det},E_{ex},T)e^{-i\Delta\phi_0} + A_{2D}^{NR}(E_{det},E_{ex},T)e^{+i\Delta\phi_0}. \quad \text{(S35)}$$

Now, the rephasing and non-rephasing signals can be retrieved by recording complex-valued A_{2D}^{+} 2DES spectra for two different values of $\Delta\phi_0$ and by linearly superimposing these spectra [16]. When choosing absolute phase values $\Delta\phi_0 = [0, \pi/2]$, the 2DES spectrum with $\Delta\phi_0 = \pi/2$ needs to be multiplied with amplitude factors of $\pm i$ to isolate A_{2D}^{R} and A_{2D}^{NR}.

$$A_{2D}^{R}(E_{det},E_{ex},T) = A_{2D}^{+}(E_{det},E_{ex},T;0) + iA_{2D}^{+}(E_{det},E_{ex},T;\pi/2)$$
$$A_{2D}^{NR}(E_{det},E_{ex},T) = A_{2D}^{+}(E_{det},E_{ex},T;0) - iA_{2D}^{+}(E_{det},E_{ex},T;\pi/2). \quad \text{(S36)}$$

Amplitude factors of $\mp i$ are needed when choosing $\Delta\phi_0 = [0, -\pi/2]$. Conventional, non-phase-cycled absorptive 2DES maps are obtained by setting $\Delta\phi_0 = 0$. From these 2DES scans, A'_{2D} are then calculated using Eq. (S32) without causality enforcement. A_{2D}^{+} are then deduced according to Eq. (S33). This yields a superposition of the non-rephasing signal with the complex conjugate of the rephasing signal (R*+NR). While this does not affect the real part of the map, the imaginary part does show a different phase twist compared to the "true" absorptive map comprising the non-conjugated rephasing signal (see Eq. (S34) for $\Delta\phi_0 = 0$) as demonstrated in Fig. S3.

4.4 0Q and 2Q spectra

For the 0Q and 2Q spectra, the data points recorded at the negative half of the τ axis are used [17]. Hence, after enforcing causality along the detection time t axis (Eq. (S32)), the data have to be flipped along τ. We then ensure a strict - albeit reversed - pulse ordering in analogy to Eq. (S35). The 0Q and 2Q spectra reported in the main text show no waiting time dependence since the waiting time is fixed to $T = 0$,

$$A_{2D}^{-}(E_{det},E_{ex};\Delta\phi_0) = \int_{-\infty}^{\infty} \Theta(\tau)\delta R'(E_{det},-\tau,T=0;\Delta\phi_0)e^{+i\frac{E_{ex}}{\hbar}\tau}\mathrm{d}\tau\,. \quad \text{(S37)}$$

The interaction with the pump pulses imprints the same phases onto the 0Q and 2Q signals as in the case of the rephasing and non-rephasing signals in Eq. (S34). As for the 1Q signals, residual phases $\delta\phi(E_{ex})$ can be corrected, leaving

$$A_{2D}^{-}(E_{det},E_{ex},T;\Delta\phi_0) = A_{2D}^{0Q}(E_{det},E_{ex},T)e^{-i\Delta\phi_0} + A_{2D}^{2Q}(E_{det},E_{ex},T)e^{+i\Delta\phi_0}. \tag{S38}$$

Analog to Eq. (S36), we calculate linear superpositions of the two datasets to obtain preliminary 0Q/2Q spectra [17]. Again, for $\Delta\phi_0 = [0, -\pi/2]$, $\mp i$ would be required, instead.

$$\begin{aligned} A_{2D}^{0Q}(E_{det},E_{ex}) &= A_{2D}^{-}(E_{det},E_{ex};0) + iA_{2D}^{-}(E_{det},E_{ex};\pi/2), \\ A_{2D}^{2Q}(E_{det},E_{ex}) &= A_{2D}^{-}(E_{det},E_{ex};0) - iA_{2D}^{-}(E_{det},E_{ex};\pi/2). \end{aligned} \tag{S39}$$

In contrast to the 1Q signals, the signal emission, which starts with the last pulse interaction, i.e. pump pulse 1, is now delayed by $T + \tau$ compared to the probe pulse that acts as the local oscillator in the measurement. Thus, an additional linear phase is imprinted on the measured spectra that reflects this relative delay. Due to this phase, equal for 0Q and 2Q signals, the measurement is effectively performed in a rotating frame at the detection frequency [17]. Thus, the correct signals are retrieved after shifting the data up by the detection frequency,

$$E_{0Q/2Q} = E_{ex} + E_{det}. \tag{S40}$$

Note, that the 2DES signal is, for the NR and R as well as for the uncorrected 2Q and 0Q spectra, located in the (E_{det},E_{ex}) and $(E_{det}, -E_{ex})$ quadrants, respectively. The corrected 0Q spectrum is hence located close to $(E_{det},E_{0Q} \approx 0)$ and the corrected 2Q signal at $(E_{det},E_{2Q} \approx E_{ex} + E_{det})$.

5. Imaginary parts of 2DES spectra for ProSQ-C16 J-aggregates

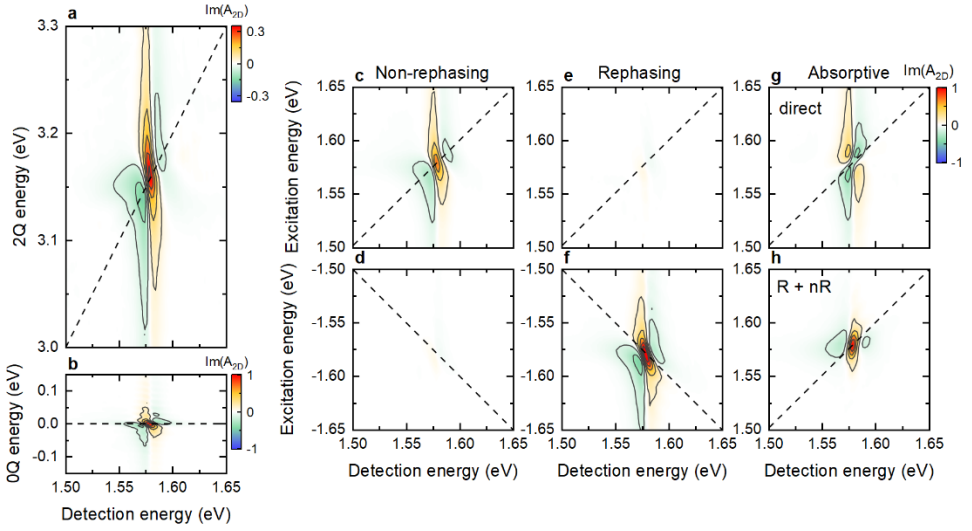

Fig. S3: Imaginary parts of the measured 2DES spectra for the molecular J-aggregate sample. Phase cycling allows to obtain 2Q (a), 0Q (b), non-rephasing (c,d) and rephasing (e,f) spectra. The sum of rephasing and non-rephasing (R+nR) (h) does not match the measured data (g) for the absorptive map, since it corresponds to (R*+nR).

6. Rephasing and non-rephasing spectra of HITCI dye in ethanol

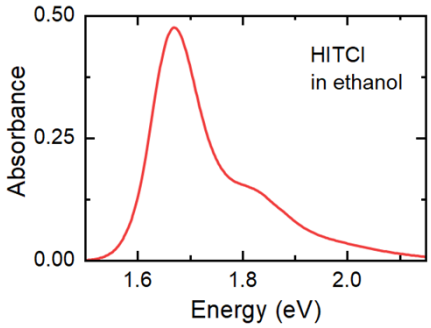

Fig. S4: Linear absorption spectrum of HITCI dye dissolved in ethanol, measured in a 1 mm cuvette.

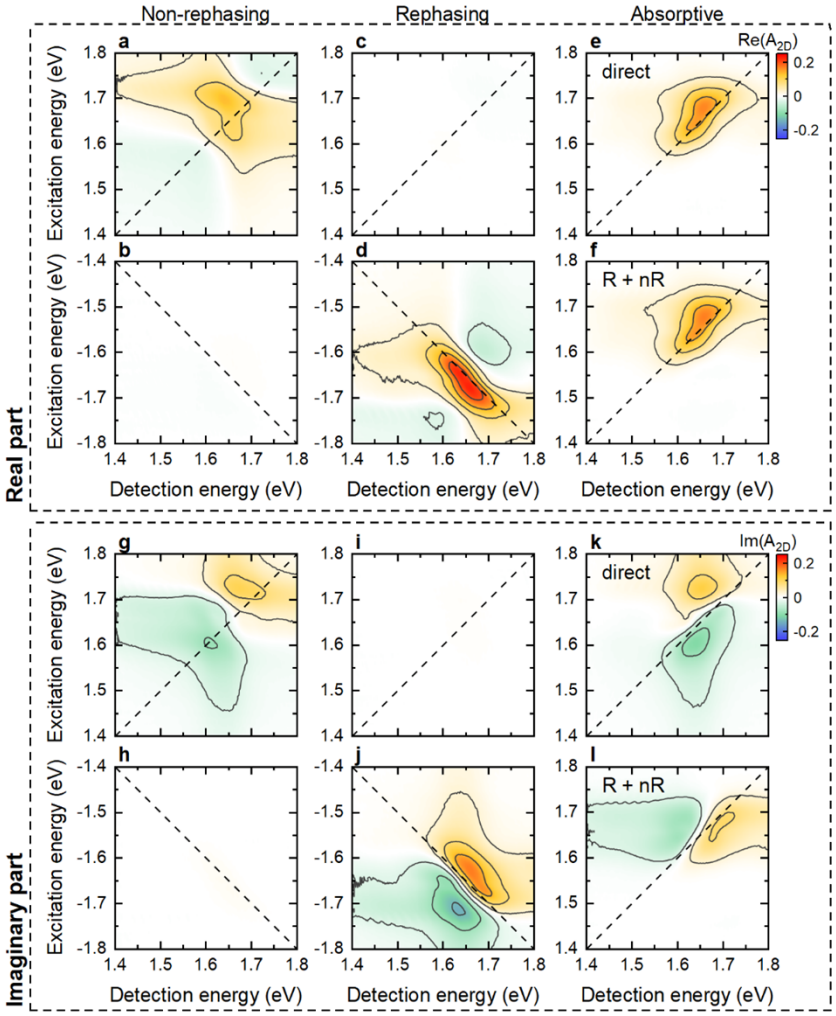

Fig. S5: Experimental results for 2DES on HITCI dissolved in ethanol for T = 200 fs. (a)-(f) Real parts of the non-rephasing (a,b), rephasing (c,d) and absorptive (e,f) spectra obtained by phase cycling. (g)-(l) Corresponding Imaginary

References

1. J. Réhault, M. Maiuri, C. Manzoni, et al., "2D IR spectroscopy with phase-locked pulse pairs from a birefringent delay line," Opt. Express **22**, 9063-9072 (2014).
2. D. Brida, C. Manzoni, and G. Cerullo, "Phase-locked pulses for two-dimensional spectroscopy by a birefringent delay line," Opt. Lett. **37**, 3027-3029 (2012).
3. J. Réhault, M. Maiuri, A. Oriana, et al., "Two-dimensional electronic spectroscopy with birefringent wedges," Rev. Sci. Instrum. **85**(2014).
4. E. Hecht, *Optics* (Pearson Education India, 2012).
5. P. S. Theocaris and E. E. Gdoutos, *Matrix theory of photoelasticity* (Springer, 2013), Vol. 11.
6. D. C. Lünemann, A. R. Thomas, J. Xu, et al., "Distinguishing between coherent and incoherent signals in excitation-emission spectroscopy," Opt. Express **29**, 24326-24337 (2021).
7. P. Hamm and M. Zanni, *Concepts and methods of 2D infrared spectroscopy* (Cambridge University Press, 2011).
8. S. Mukamel, *Principles of nonlinear optical spectroscopy*, Oxford series in optical and imaging sciences (Oxford University Press, New York, 1995), pp. xviii, 543 p.
9. H. Li, B. Lomsadze, G. Moody, et al., *Optical Multidimensional Coherent Spectroscopy* (Oxford University Press, 2023).
10. M. Sargent, M. O. Scully, and W. E. Lamb, *Laser physics* (Addison-Wesley Pub. Co., Advanced Book Program, Reading, Mass.,, 1974), p. 432 p.

11. T. Quenzel, D. Timmer, M. Gittinger, et al., "Plasmon-Enhanced Exciton Delocalization in Squaraine-Type Molecular Aggregates," Acs Nano **16**, 4693-4704 (2022).
12. A. Grupp, A. Budweg, M. P. Fischer, et al., "Broadly tunable ultrafast pump-probe system operating at multi-kHz repetition rate," J. Optics **20**(2018).
13. D. Timmer, M. Gittinger, T. Quenzel, et al., "Plasmon mediated coherent population oscillations in molecular aggregates," Nat. Commun. **14**(2023).
14. G. Stibenz and G. Steinmeyer, "Interferometric frequency-resolved optical gating," Opt. Express **13**, 2617-2626 (2005).
15. J. H. Zhong, J. Vogelsang, J. M. Yi, et al., "Nonlinear plasmon-exciton coupling enhances sum-frequency generation from a hybrid metal/semiconductor nanostructure," Nat. Commun. **11**(2020).
16. J. A. Myers, K. L. M. Lewis, P. F. Tekavec, et al., "Two-color two-dimensional Fourier transform electronic spectroscopy with a pulse-shaper," Opt. Express **16**, 17420-17428 (2008).
17. M. R. Cai, X. Zhang, Z. Q. Cheng, et al., "Extracting double-quantum coherence in two-dimensional electronic spectroscopy under pump-probe geometry," Rev. Sci. Instrum. **95**(2024).